

# Investigation of tDCS volume conduction effects in a highly realistic head model

S.Wagner<sup>\*,1,#</sup>, S.M. Rampersad<sup>\*,2</sup>, Ü. Aydin<sup>1</sup>, J. Vorwerk<sup>1</sup>, T.F. Oostendorp<sup>2</sup>, T. Neuling<sup>3</sup>, C.S. Hermann<sup>3</sup>, D.F. Stegeman<sup>2,4</sup> and C.H. Wolters<sup>1</sup>

- 1) Institute for Biomagnetism and Biosignalanalysis, University of Münster, Münster, Germany
- 2) Radboud University Nijmegen Medical Centre, Donders Institute for Brain, Cognition and Behaviour, Nijmegen, The Netherlands
- 3) Experimental Psychology Lab, Center for Excellence "Hearing4all", European Medical School, University of Oldenburg, Oldenburg, Germany
- 4) Research Institute MOVE, Faculty of Human Movement Sciences, VU University, Amsterdam, The Netherlands

\*The first two authors contributed equally to this work.

#Correspondence to: Sven Wagner, Institute for Biomagnetism and Biosignalanalysis, University of Münster, Malmedyweg 15, 48149 Münster. Tel. +49 (0)251-83-52413, Fax. +49 (0)251-83-56874. Email: sven.wagner@uni-muenster.de

## Key words

Transcranial direct/alternating current stimulation (tDCS/tACS); simulation study; finite element method; realistic head model; volume conduction effects; skull modeling; white matter conductivity anisotropy; guideline for tDCS head modeling

## Abstract

### Objective

We investigate volume conduction effects in transcranial direct current stimulation (tDCS) and present a guideline for efficient and yet accurate volume conductor modeling in tDCS using our newly-developed finite element approach.

### Approach

We developed a new, accurate and fast isoparametric FE approach for high-resolution geometry-adapted hexahedral meshes and tissue anisotropy. To attain deeper insight into tDCS, we performed computer simulations, starting with a homogenized three-compartment head model and extending this step by step to a six-compartment anisotropic model.

### Main Results

We are able to demonstrate important tDCS effects: First, we find channeling effects of the skin, the skull spongiosa and the cerebrospinal fluid compartments. Second, current vectors tend to be oriented towards the closest higher conducting region. Third, anisotropic WM conductivity causes current flow in directions more parallel to the WM fiber tracts. Fourth, highest cortical current magnitudes are not only found close to the stimulation sites. Fifth, median brain current density decreases with increasing distance to the electrodes.

### Significance

Our results allow us to formulate a guideline for volume conductor modeling in tDCS. We recommend to accurately model the major tissues between the stimulating electrodes and the target areas, while for efficient yet accurate modeling, an exact representation of other tissues is less important. Because for the low-frequency regime in electrophysiology, the quasi-static approach is justified, our results should also be valid for at least low-frequency (e.g., below 100Hz) transcranial alternating current stimulation (tACS).

## Introduction

Transcranial direct current stimulation (tDCS) is a non-invasive, painless, easy-to-perform and inexpensive brain stimulation technique using mostly relatively large electrodes attached to the scalp (Nitsche and Paulus, 2000; Zaehle et al., 2010). A small (0.5-2 mA) or low intensity (< 0.5 mA, see, e.g., Jäger et al.,

1987; Marshall et al., 2005) current is introduced to the human head by at least one electrode (anode) and removed at another (cathode). This current can increase or decrease cortical excitability in regions of interest, dependent on the polarity of the current (Nitsche and Paulus, 2000). This non-invasive technique to stimulate the brain can be exploited to achieve beneficial effects in neuropsychiatric or neurological disorders such as Alzheimer's disease (Ferrucci et al., 2008), Parkinson's disease (Boggio et al., 2006) and epilepsy (Fregni et al., 2006). Furthermore, tDCS can enhance cognitive functions (Iyer et al., 2005) and facilitate motor rehabilitation after stroke (Hummel et al., 2005). For these reasons, interest in tDCS as a tool for both clinical and neuroscientific research has been growing substantially over the past two decades.

Besides the progress in the use of tDCS in practical experiments, important steps have been made by the use of computational models that are able to simulate the electric field resulting from tDCS. A final goal of modeling brain stimulation is to have patient-specific models in order to predict personally optimized stimulation protocols. Due to recent advances in computational possibilities and improved imaging and modeling methods, this goal is becoming more reachable every day. However, the difficulty in creating such models is finding the balance between fast production and accuracy. Therefore, it is necessary to know what the crucial aspects are with respect to accuracy: which tissue compartments are more and which are less important and what is the required amount of detail needed in each compartment?

In the past, spherical shell models with three or more compartments have been used for tDCS simulation (Miranda et al., 2006; Rampersad et al., 2012a). An important step was the investigation of MRI-derived finite element (FE) head models for brain stimulation. Models using separate skull layers (Holdefer et al., 2006; Rampersad et al., 2012a), the highly conductive CSF compartment (Wagner et al., 2007; Salvador et al., 2010; Datta et al., 2011; Parazzini et al., 2012), a white matter compartment (Wagner et al., 2007; Parazzini et al., 2011; Sadleir et al., 2010; Salvador et al., 2012) and white matter anisotropy (Holdefer et al., 2006; Oostendorp et al., 2008; Suh et al., 2009; Sadleir et al., 2012) have been employed. There is no doubt that each of the above studies assisted in gaining insight into tDCS. However, the sophisticated interplay between stimulation and cortical current density distribution in the individual and the sensitivity of it towards the most important tissue compartments is still rather vague. Our study intends to shed more light on it. We propose to start with a low-parametric homogenized three-compartment (skin, skull, brain) head model and to extend it step by step to a more realistic anisotropic six-compartment model. In this way, we are able to interpret each effect individually, enabling a new level of understanding of tDCS volume conduction effects and allowing us to provide suggestions as to which factors are the most important to include in individual head models.

Our tDCS FE implementation, developed by Wagner (2011) and for the first time presented in more detail in this study, not only has a resolution of over two million of FE nodes, but also allows curved boundaries in a hexahedral model. Motivated by a similar approach for EEG source analysis (Wolters et al., 2007), we developed an isoparametric (i.e., the finite element basis functions are not only used for potential approximation, but additionally for an improved description of the element contours) FE approach for tDCS stimulation that is specifically tailored to geometry-adapted hexahedral meshes, resulting in significantly reduced numerical errors (Wagner, 2011).

While modeling multiple isotropic tissue compartments in realistic head models segmented from registered T1-weighted (T1w) and T2w MRIs is becoming a more and more standardized procedure (Windhoff et al., 2011; Dannhauer et al., 2011; Datta et al., 2011), accurate modeling of white matter conductivity anisotropy is still a challenging task. As suggested by (Basser et al., 1994; Tuch et al., 2001; Rullmann et al., 2009),

conductivity tensors can be computed from measured diffusion-tensor MRI (DT-MRI). However, DT-MRI data suffer from geometrical distortions and intensity modulations because of susceptibility artifacts which complicate its fusion with T1w or T2w datasets. Here, we employ a new nonlinear registration method that uses a reversed gradient approach based on images acquired in positive and negative phase-encoding direction (Ruthotto et al., 2012). In this way, smooth and diffeomorphic transformations are computed to correct for susceptibility artifacts enabling an adequate fusion with the T1w and T2w images during the head model setup procedure.

The model presented here combines properties that, to the best of our knowledge, have not been used together in such detail in tDCS simulations before. This model was used to create realistic predictions of tDCS results for two commonly targeted areas. While the focus of our investigation is on a frequently used tDCS configuration for auditory cortex stimulation, we also present our main results for motor cortex stimulation. Additionally, we use a step-by-step approach in order to improve understanding of tDCS volume conduction effects. In each step, the effect of the increased realism in volume conductor modeling on the tDCS current density is investigated by means of high-resolution vector field visualization and quantification of field changes in orientation and magnitude. Our study concludes with guidelines for efficient and yet accurate volume conductor modeling for tDCS.

## Methods

First, the generation of the MRI-based head model and the localization of auditory and motor cortex will be depicted. Then we describe our tDCS modeling pipeline and the calculation of the current density within the whole volume conductor model. Finally, the different head models used in our step-by-step approach and the measures for the quantification of the differences are introduced.

### Measurement of MRI

T1-, T2- and diffusion-weighted MRI scans of a healthy 26-year-old male subject were measured on a 3T scanner (Gyroscan Intera/Achieva 3.0T, System Release 2.5 (Philips, Best, NL)). The subject signed the written consent form and the procedures were approved by an ethical committee. A T1w pulse sequence with water selective excitation and a T2w pulse sequence with minimal water-fat-shift were used, both with an isotropic resolution resulting in cubic voxels of 1.17 mm edge length. This resolution will also define our FE mesh resolution used throughout this study. Diffusion weighted MRI was performed using a Stejskal-Tanner spin-echo EPI sequence with a SENSE parallel imaging scheme in AP direction (acceleration factor 2). Geometry parameters were: FOV 240 mm x 240 mm for 70 transverse slices, 1.875 mm thick, without gap, with a square matrix of 128, resulting in cubic voxels of 1.875 mm edge length. Contrast parameters were TR = 7546 ms, TE = 67 ms. One volume was acquired with diffusion sensitivity  $b=0$  s/mm<sup>2</sup> and 20 volumes with  $b=1000$  s/mm<sup>2</sup> using diffusion weighted gradients in 20 directions, equally distributed on a sphere according to the scheme of (Jones, 2004). The pixel bandwidth was 2873 Hz/pixel and the bandwidth in the phase encoding direction was 20.3 Hz/pixel. An additional volume with flat diffusion gradient, i.e.,  $b=0$  s/mm<sup>2</sup>, was acquired with reversed encoding gradients to later use in susceptibility correction.

### Registration and segmentation of T1w and T2w MRI

The T2w MRI was registered onto the T1w MRI using a rigid registration approach and mutual information

(Maes et al., 1997) as a cost-function as implemented in FSL<sup>1</sup>. Then, brain, inner skull, outer skull and skin masks were obtained from the T1w and T2w images. In a next step, the T1w image served for the segmentation of gray and white matter and the T2w image for the segmentation of the CSF. For all of these steps, the FSL software was used (Jenkinson et al., 2012). The segmentation was visually inspected and manually corrected using CURRY<sup>2</sup>. Segmentation of the skull spongiosa was based on the T2w image. The skull was first constrained using the inner and outer skull masks on the T2w MRI and then a one-voxel-erosion was performed on the skull compartment (this will later guarantee that inner and outer skull compacta are at least one voxel thick (Akhtari et al., 2002)). Finally, a thresholding based region-growing segmentation constrained to the eroded skull compartment was used to differentiate between spongiosa and compacta again using CURRY.

### **Localization of auditory and motor cortex**

For appropriate placement of the electrodes, we localized both auditory and motor cortex of the subject of this study using 275 channel magnetoencephalography (MEG) experiments.

For localization of the auditory cortex, we performed a source analysis of the measured auditory evoked fields (AEF) and calculated the dipole solution for the auditory N1 component from the averaged AEF using CURRY. We performed another source analysis to localize the somatosensory N20 component in the posterior wall of the central sulcus and, using this landmark, identified the motor cortex in the nearby anterior wall of the central sulcus.

These localization results were used to position the center of the anode (see further description below and Figs.1-A2, S1-A2) and to determine the location of coronal cut planes for visualization of the simulation results (see Figs.1, 2, 5 and S1).

### **Modeling of anode and cathode**

Two tDCS electrodes were modeled as rectangular patches with a commonly used size of 7 cm x 5 cm (Fregni et al., 2006; Zaehle et al., 2010), thickness of 4 mm and conductivity of 1.4 S/m (Sadleir et al., 2010; Datta et al., 2011) and a total current of 1 mA was applied. To simulate auditory cortex stimulation, the patches were positioned symmetrically around the localized auditory cortex above the area of the TP9, TP10, P7, P8, T7, T8, CP5 and CP6 electrodes using the conventions of a standard 10/10 EEG system, as can be seen in Fig. 1-A2 and -A3. We modeled the anode over the right hemisphere and the cathode over the left hemisphere. For the motor stimulation scenario, the anode was placed above the localized left primary motor cortex (M1) and the cathode above the right eyebrow (Nitsche and Paulus, 2000) (Fig. S1-A2 and -A3).

### **Generation of the geometry-adapted hexahedral finite element mesh**

A hexahedral finite element mesh was constructed out of the labeled volume. To increase conformance to the real geometry and to mitigate the staircase effects of a voxel mesh, we applied a technique to shift nodes on material interfaces (Camacho et al., 1997; Wolters et al., 2007). We chose a nodeshift factor of 0.33, which ensured that interior angles at element vertices remained convex and the Jacobian determinant in the

---

<sup>1</sup> <http://www.fmrib.ox.ac.uk/fsl>.

<sup>2</sup> <http://www.neuroscan.com/curry.cfm>

FEM computations remained positive. This procedure resulted in a geometry-adapted hexahedral FE mesh with 2,2M nodes and 2,2M elements. The freely available software SimBio-VGRID<sup>3</sup> was used for mesh generation.

### **Inclusion of white matter conductivity tensors**

Basser et al. (1994) and Tuch et al. (2001) introduced the assumption that conductivity tensors can be derived from non-invasively measured DT-MRI. Positive validations of this model were reported by Tuch et al. (2001) and Oh et al. (2006). We followed this procedure as described in the following: Our diffusion-weighted (DW) MR images were corrected for eddy current (EC) artifacts by affine registration of the directional images to the b0 image using the FSL routine FLIRT. After this procedure, the gradient directions were reoriented using the rotational part of the transformation matrices obtained in the EC correction scheme. Then, our new diffeomorphic approach for the correction of susceptibility artifacts using a reversed gradient approach and multiscale nonlinear image registration was applied to the DW-MRI datasets (Ruthotto et al., 2012). This approach is implemented in the freely-available SPM<sup>4</sup> and FAIR<sup>5</sup> software packages. After EC and susceptibility correction, the b0 image was rigidly registered to the T2w image using FLIRT and the transformation matrix obtained in this step was used for the registration of the directional images, while taking care that the corresponding gradient directions were also reoriented accordingly. The tensors were then calculated using the FSL routine DTIFIT (Jenkinson et al., 2012). In a last step, white matter conductivity tensors were calculated from the artifact-corrected and registered diffusion tensor MR images using the effective medium approach as described in (Tuch et al., 2001) and embedded in the geometry-adapted hexahedral FE head model. The scaling factor between diffusion and conductivity tensors was selected so that the arithmetic mean of the volume of all white matter conductivity tensors optimally fits the volume of the isotropic approximations in a least squares sense (Rullmann et al., 2009).

### **Finite element method based tDCS modeling**

For modeling tDCS, the quasi-static approximation to Maxwell's equations for computing the electric field is justified, because in the considered low-frequency regime of electrophysiology, capacitive, inductive and propagation effects can mainly be neglected (Plonsey and Heppner, 1967; Hämäläinen et al., 1993; Logothetis et al., 2007). This yields the Laplace equation  $\nabla \cdot (\sigma \nabla \varphi) = 0$  with  $\sigma$  being the conductivity tensor and  $\varphi$  being the electric potential and inhomogeneous Neumann boundary conditions at the electrode surfaces and homogeneous Neumann boundary conditions for the remaining model surface (Sadleir et al., 2010). For the numerical approximation of the potential in tDCS simulation, a geometry-adapted hexahedral finite element approach with isoparametric transformations of deformed (at tissue boundaries, as discussed) cubic elements to the reference cube element and piecewise trilinear basis functions was implemented (Wagner, 2011). For an efficient solution of the tDCS FE equation system, we used an algebraic multigrid preconditioned conjugate gradient (AMG-CG) iterative solver method that is specifically appropriate for inhomogeneous and anisotropic head volume conductor models (see section 4.5 "Comparison of arithmetic

---

<sup>3</sup> The SimBio-Vgrid mesh generator: <http://www.rheinahrcampus.de/~medsim/vgrid/index.html>

<sup>4</sup> SPM extension toolbox ACID (Algorithm HySCo): see <http://www.fil.ion.ucl.ac.uk/spm/ext/> and <http://www.diffusiontools.com/HySCo.html>

<sup>5</sup> Flexible Algorithms for Image Registration (FAIR): <http://www.mic.uni-luebeck.de/people/jan-modersitzki/software/fair.html>

operations" for the adjoint approach in (Wagner, 2011)). The implemented numerical approach was validated for tDCS simulations in multi-layer sphere modeling scenarios, where analytical solutions exist (de Munck and Peters, 1993). Significant error reductions compared to regular hexahedral approaches were shown, leading to high numerical accuracies especially for high-resolution meshes (see accuracies of the adjoint approach in Figs.5.9 and 5.10 in Wagner (2011)). We used our freely available SimBio<sup>6</sup> software toolbox for all FEM implementations and computations. From the approximated potential at the nodes, we computed the current density  $\vec{J} = \sigma \nabla \Phi$  in all elements of the volume conductor via fast routines implemented in SimBio.

## Setup of the head models

Please put < Table 1 > here!

### *Three-compartment isotropic head model (3CI)*

The most homogenized model is the classic three-compartment (skin, skull, brain) model (Miranda et al., 2006) that is denoted by head model 3CI in our investigations. In the related field of EEG forward modeling, this low-parametric approach is still the most-widely used (see Dannhauer et al. (2011) and references therein). The brain compartment is defined as the region inside the interior skull surface, the skull as the region between the interior and exterior skull surface and the skin as the region outside the exterior skull surface. For the skin, skull and brain compartments, we used isotropic conductivity values of 0.43 S/m, 0.01 S/m and 0.33 S/m, respectively (Dannhauer et al., 2011; Ramon et al., 2004). The value of 0.01 S/m for the skull was chosen both to be in the range of the values that best approximated the more realistic compacta/spongiosa-structure of the skull (Dannhauer et al., 2011) and to be identical to the skull conductivity used in other tDCS simulation studies (Wagner et al., 2007; Datta et al., 2011; Dmochowski et al., 2011).

### *Four-compartment isotropic head model (4CI)*

The four-compartment head model 4CI incorporates skull spongiosa and compacta instead of a homogenized version of the skull compartment as used in model 3CI. Akhtari et al. (2002) measured the conductivities of live human skull fragments and found average conductivity values of 0.007 S/m for the compacta and 0.025 S/m for the spongiosa, which we used for this study.

### *Five-compartment isotropic head model (5CI)*

The highly conductive CSF with isotropic conductivity of 1.79 S/m (Baumann et al., 1997) was added to the 4CI model, resulting in model 5CI.

### *Six-compartment isotropic head model (6CI)*

Model 6CI distinguishes between brain gray and white matter using isotropic conductivity values of 0.33 S/m

---

<sup>6</sup> SimBio: A generic environment for bio-numerical simulations, see <http://www.simbio.de/> and <https://www.mrt.uni-jena.de/simbio>.

and 0.14 S/m, resp. (Ramon et al., 2004).

#### *Six-compartment head model with anisotropic white matter compartment (6CA)*

Model 6CA incorporates white matter conductivity anisotropy as described above.

#### **Visualization of the current density vector fields**

For the visualization of the vector fields, we use size-normalized cones to represent vector orientations and color-coded cones to represent their amplitudes. All computations are performed on the highest resolution meshes, a resolution that can only be visualized completely if we zoom into details (see Fig. 4) and is too fine for visualization of the field over a whole cut plane. Therefore, thinned versions of the calculated vector fields are presented, where only the middle cone of each 4 x 4 FE element block is visualized (see, e.g., left column in Fig. 1).

Additionally, we compute the change in orientation *Ang* (degree) and the change in amplitude *Mag* (factor) for each incorporated feature (see, e.g., Columns 2 and 3 in Fig. 1) as follows:

$$Ang(i) = \arccos \frac{\langle \vec{J}_1(i), \vec{J}_2(i) \rangle}{\|\vec{J}_1(i)\| \|\vec{J}_2(i)\|} \quad (1)$$

$$Mag(i) = \frac{\|\vec{J}_2(i)\|}{\|\vec{J}_1(i)\|} \quad (2)$$

with  $\vec{J}_1(i)$  and  $\vec{J}_2(i)$  being the calculated current densities in the reference and expanded models in the *i*-th element, respectively.

As a measure of directional agreement between the fiber directions in the brain and the calculated current densities, we calculate the parallelity *Par*:

$$Par(i) = \cos(\langle \vec{J}(i), \vec{v}(i) \rangle) \quad (3)$$

with  $\vec{v}(i)$  the primary eigenvector of the conductivity tensor in the *i*-th element. A *Par* value of 1 indicates directional similarity, whereas 0 represents orthogonality.

All visualizations in this study were carried out using the software SCIRun<sup>7</sup>.

## **Results**

We will first present the current density distribution in the isotropic three-compartment head model and then expound on the changes in current density that occur as we extend the low-parametric model step by step to a more realistic anisotropic six-compartment head model. As the results for auditory and motor cortex stimulation did not essentially differ, we present only figures for auditory cortex stimulation here. For motor

<sup>7</sup> SCIRun: A Scientific Computing Problem Solving Environment, Scientific Computing and Imaging Institute (SCI), <http://www.scirun.org>.

cortex stimulation, we will discuss only the main differences with respect to auditory stimulation; an additional figure (Fig. S1) can be found in the Supplementary Material, which is available online.

### **Isotropic three-compartment model (3CI model)**

Please put Figure 1 here!

In Fig. 1-A1 we present the current density distribution in the 3CI model as a vector field. Peak current densities of  $1.2 \text{ A/m}^2$  are found in the skin at the edges of the electrodes. Most of the current that enters the skin is deflected by the low conductive skull and tangentially channeled along the skin from anode to cathode, while minor currents penetrate the skull with mainly radial orientation. The isotropic brain compartment leads to a homogeneous current density distribution inside the interior skull surface. Fig. 1-A1 is scaled to the full range of values in the complete model, rendering some of the variations in the brain indistinguishable.

Please put Figure 2 here!

For this reason, an identically structured plot showing only the brain compartment is presented in Fig. 2-A1. Peak cortical current densities of  $0.11 \text{ A/m}^2$  occur in regions directly underneath the tDCS electrodes.

Please put Figure 3 here!

Fig. 3 demonstrates the interplay of current density amplitude within the brain and distance to the nearest electrode node. A correlation between distance and decrease in amplitude can be seen, that is, the current density in the 3CI model decreases smoothly into brain regions that are farther away from the electrodes.

### **Including the layered skull structure (4CI model)**

The first feature added to the 3CI model was the distinction between skull compacta and spongiosa. In Figs. 1-B (whole model) and 2-B (only brain compartment), the consequences of this expansion for the current density distribution were characterized. In the first column (Figs. 1-B1 and 2-B1) we present the current density vector field of the 4CI model. The second (Figs. 1-B2 and 2-B2) and third (Figs. 1-B3 and 2-B3) columns display differences in current density orientation (Ang, Eq. 1) and magnitude (Mag, Eq. 2) between the 3CI model and the 4CI model. Changes in orientation of up to 64 degrees can be observed in the skull, while minor changes are visible in the skin and brain. Because of the conduction increase in spongiosa, orientation changes (up to 9.2 degrees) do occur in the cortex, mostly in brain regions underneath spongiosa. This means that for auditory cortex stimulation (A1) the target area is hardly affected (Fig. 2-B2), while for motor cortex stimulation (M1) the largest orientation changes (up to 12 degrees) were found in the target area (Fig. S1-B2).

The current density decreases ( $\text{Mag} < 1$ ) in the whole brain and in most compacta regions (Figs. 2-B3 and 1-B3). An increase in magnitude ( $\text{Mag} > 1$ ) can be seen in the lower resistive spongiosa compartment (Fig. 1-B3) and in a cortical region underneath a large patch of spongiosa above the motor cortex stimulation site (Fig. S1-B3). The locations of the peak cortical current density did not shift with respect to the 3CI model in



A1 (Fig. 2-B1) and only showed slight changes in M1 stimulation.

Fig. 3 shows a correlation between distance and decrease in brain current density similar to what was seen in the 3CI model.

Please put Figure 4 here!

The vector field in a region containing major changes in orientation (red box in Fig. 1-B1) is displayed in full resolution in Fig. 4-A. In the skull, mainly radial orientation of the current can be seen in the 3CI head model (Fig. 4-A1), while far more tangentially oriented components occur in the 4CI model (Fig. 4-A2) due to the 3.6 times higher conductivity of spongiosa compared to compacta (averaged ratio of Akhtari et al. (2002)). When using the maximal reported ratio of 1:8.2 of Akhtari et al. (2002) (Fig. 4-A3), a correlation between the ratio and the tangential behavior of the vectors in the spongiosa layer can be observed. To obtain mainly tangential components of the current density within the spongiosa, a ratio of 1:23 was required (Fig. 4-A4). The compacta-to-spongiosa conductivity ratio thus influences the direction of the current in the spongiosa, resulting in a tangential channeling effect for high ratios, which in case of M1 stimulation also significantly affected the current density in the target brain area (Fig. S1-B2,B3).

#### **Including the CSF compartment (5CI model)**

Incorporating the highly conductive CSF medium into the 4CI head model influences the orientation in the skull, CSF (up to 75 degrees, Fig. 1-C2) and brain (up to 44 degrees, Fig. 2-C2). In the brain, modifications with regard to orientation are found in most cortical regions bordering CSF.

Due to a significant increase in conductivity, the current density in CSF increases by a factor of up to 6.1 as compared to the value in the 4CI model (Fig. 1-C3). On the contrary, current density decreases in white matter and in most cortical regions, especially close to the stimulation site (Fig. 2-C3). Lesser changes are visible in the skull and there is hardly any change in the skin compartment.

Fig. 3 demonstrates that the current density in the 5CI model decreases for an increase in distance, except the region between distances 10 and 15 mm where amplitude decreases slightly. Compared to model 4CI, there is a decrease in current density of about 50% in brain areas close to the electrodes and a smaller decrease farther away along with a significant increase in maximal amplitude in faraway regions.

Major changes in orientation due to the CSF are illustrated in Fig. 4-B, showing the vector field in the 4CI (Fig. 4-B1,B3) and 5CI (Fig. 4-B2,B4) models at two locations (red boxes areas in Fig. 1-C1). A big amount of the current that has passed the skull underneath the anode is channeled along the CSF towards more faraway areas (Fig. 4-B2). The bottom row of Fig. 4-B shows a sulcus in both the 4CI (Fig. 4-B3) and the 5CI (Fig. 4-B4) model. Contrary to the homogeneous current density seen in the 4CI model, the current travels mainly along and towards the CSF here, leading to higher current amplitudes in the sulci and to an overall more irregular pattern of peak cortical current density (Fig. 2-C1).

#### **Differentiating between gray and white matter (6CI model)**

Fig. 1-D1 displays the current density vector field in a model in which gray and white matter are modeled as separate compartments. As can be seen in Fig. 1-D2, orientation changes (up to 28 degrees) occur mostly near the boundary between gray and white matter and in inferior parts of the CSF. Figs. 1-D3 and 2-D3 show an increase in current density in the CSF and a decrease in white matter. In the gray matter, current density

decreases slightly close to the site of stimulation and increases farther away. In Fig. 3 we see that the median current density in the whole brain does not change much close to the electrodes, but decreases farther away.

Fig. 4-C depicts two brain regions including gray/white matter boundaries (red boxes areas in Fig. 1-D1) within the simpler 5CI (Fig. 4-C1,C3) and the more realistic 6CI (Fig. 4-C2,C4) model. The vector field in white matter tends to be oriented towards the nearest gray matter region. This effect is not seen farther away from the gray/white matter boundaries (Fig.2-D1).

### **Adding white matter anisotropy (6CA model)**

Figs. 1-E and 2-E display the current density vector field along with orientation (Ang) and magnitude (Mag) changes after adding white matter anisotropy to the 6CI model. Orientation changes (up to 63 degrees) and magnitude changes (up to a factor of 4.5) occur in the white matter compartment and are largest in central white matter areas. In deep areas of the gray matter compartment, we find maximal orientation changes of 15 degrees. In superficial cortical areas, with 0 to 8 degrees, orientation changes are only moderate. Similar results are found for the current density magnitude which only changes moderately for superficial cortical areas, while factors between 0.5 and 1.3 can be found in deeper gray matter areas. Fig. 3 shows that for the whole brain the median current density decreases with increasing distance to the electrodes. In comparison to the 6CI model, the median slightly increased deeper in the brain (distances above 30 mm from the electrodes).

Fig. 4-D displays parts of the thalamocortical projection fibers (4-D1,D2) and pyramidal tracts (4-D3,D4) (see also red boxes in Fig. 1-E1) in the 6CI (4-D1,D3) and 6CA (4-D2,D4) models. In both areas, the current density flows mostly homogeneous in the isotropic model, while major changes in orientation occur in the anisotropic model.

Please put Figure 5 here!

Fig. 5 depicts the directional agreement (Par, eq. 3) between the simulated current densities and the main fiber directions in the white matter compartment (i.e., the first eigenvector of the conductivity tensor). The current density in the 6CA model (Fig. 5-B) is oriented far more parallel to the pyramidal tract, whereas the current flow in the 6CI model (Fig. 5-A) does not show much directional agreement in this area. Fig. 5-C, where for C we computed the difference of B and A (i.e.,  $C=B-A$ ), shows large differences in parallelity in central white matter areas.

## **Discussion and conclusion**

Our study has demonstrated that simulation studies in realistic MRI-derived FE head models are indispensable for the understanding of the complicated interaction of stimulation, volume conduction effects and the resulting cortical current density distribution caused by transcranial direct current stimulation.

### **Skull modeling**

Our lowest-parametric head model showed mainly radial current flow in the skull, because of the low skull conductivity of 0.01 S/m. Including spongiosa in the skull changed this behavior. Currents became

tangentially channeled along the better conductive spongiosa, leading to an overall decrease in brain current density and a small effect on current distributions in the brain. While previous studies investigating the effects of separate skull layers on simulations of electrical stimulation were performed with two-dimensional (Holdefer et al., 2006) or spherical models (Rampersad et al., 2012a), this study is the first to investigate these effects in a realistic three-dimensional tDCS model.

For auditory cortex stimulation, the target area was hardly affected by the presence of the spongiosa, while for motor cortex stimulation the target area is where the orientation change was largest. This is due to the placement of the electrodes relative to the location of spongiosa inside the skull. The closer the electrodes are to the spongiosa, the more current is shunted through this compartment and the higher the change in brain current density. This indicates that realistic modeling of the human skull is important when electrodes are placed over spongiosa areas.

### **Influence of the CSF**

When including CSF, current is channeled away from the target brain area. This is due to a significantly higher conductivity of CSF compared to the brain tissue (5.4 times bigger) and is in agreement to the findings of other studies (Datta et al., 2011; Salvador et al., 2010; Wagner et al., 2007). The CSF leads the current both towards brain regions farther away and also into the deeper lying sulci. This changes the current distribution in the brain all along the CSF/brain boundary; the distribution in the brain becomes less homogeneous. In regions close to the CSF, current densities are relatively high and directed towards the CSF. Within 10 to 15 mm of the electrodes, an increase in median brain current density was demonstrated (Fig. 3). This is caused by conduction of currents from the cortical crown to the bottom of sulci underneath the electrodes, in agreement with (Salvador et al., 2010). Our study design allows us to relate the CSF effect to the effect of other tissue compartments. In this way it gets clear that, of the four added features we investigated, the addition of the CSF had by far the largest effect on the relationship between current density and distance to the electrodes. These results show that accurate modeling of the CSF compartment as well as the brain surface is very important in tDCS simulations.

### **Including white matter**

The distinction between gray and white matter increases the resistivity within the white matter compartment, leading to a strong overall decrease in current density in the white matter. As the overall brain conductivity is now lower, there is a larger conductivity disparity between CSF and brain tissue as compared to the five-compartment model. Therefore, stronger current flow can be seen in the CSF, leading to less strong currents in the brain tissue nearby the stimulation site and stronger cortical current flow in more remote regions. The direction of white matter current densities close to the cortex tends to be oriented towards the cortex, because of the less resistive pathway offered by the cortex. Because the conductivity disparity is now only slightly bigger than the disparity that was introduced by incorporating the CSF, only marginally stronger current flow can be demonstrated, resulting in a similar pattern of peak cortical current density. The distinction between gray and white matter was modeled in several other studies (Datta et al., 2011; Salvador et al., 2010; Wagner et al., 2007; Sadleir et al., 2010), but only Sadleir and colleagues (2010) described the effect of this distinction. They also reported that changing the conductivity of the white matter compartment led to small changes in current densities in the brain compartment. However, our study enables the direct comparison to the other investigated effects, important for our goal to setup a guideline for tDCS volume

conductor modeling. As the distinction between gray and white matter significantly influences the orientation and magnitude of the current flow in the whole brain, a white matter compartment should be modeled in tDCS simulations.

### **Effect of white matter anisotropy**

When adding white matter anisotropy, we only find larger gray matter current density orientation and magnitude effects in deeper regions, while effects on the more superficial cortical areas are limited. In contrast, we can report a strong increase in current density in large parts of the white matter compartment. Current flow in white matter is oriented more parallel to the main direction of the white matter fiber bundles, clearly visible especially in the pyramidal tracts and the thalamocortical projection fiber tracts (Fig. 5). This is caused by the significant increase in conduction in directions parallel to the white matter fiber bundles. In this respect, our results are in agreement with the findings of (Holdefer et al., 2006; Oostendorp et al., 2008; Suh et al., 2009). However, while we used a 3D model, the study of (Holdefer et al., 2006) was performed in 2D on a single coronal MRI section including the motor cortex with a 2D approximation of white matter conductivity anisotropy. Furthermore, we modeled patch electrodes instead of point electrodes (Holdefer et al., 2006; Suh et al., 2009) and we used the linear effective medium approach for computing white matter conductivity anisotropy, while in (Oostendorp et al., 2008; Suh et al., 2009), fixed anisotropy ratios of 1:10 longitudinally to transversally to the white matter fiber bundles were used. Lastly, with more than 2 million FE nodes (1.17 mm edge lengths), we performed high resolution geometry-adapted hexahedral FE modeling, while studies of others were based on 2D models with 150,000 triangular elements (Holdefer et al., 2006) or tetrahedral models with 147,287 (Oostendorp et al., 2008) or 160,231 FE nodes (Suh et al., 2009). To the best of our knowledge, our study is thus the first where the influence of white matter conductivity anisotropy was evaluated in a realistic 3D scenario for tDCS using high resolution FE modeling. Our results clearly demonstrate that modeling white matter anisotropy is especially important when considering deeper target regions.

### **General discussion**

Our analysis demonstrated the influence and importance of realistic volume conductor modeling for tDCS simulation. First, current density distributions were investigated with respect to orientation and strength and, second, gray matter regions receiving highest current densities were evaluated. The results clearly demonstrated that three-dimensional multi-compartment finite element head models are needed to obtain accurate tDCS current flow simulation results. While other authors allude the importance (Wagner et al., 2007; Holdefer et al., 2006; Datta et al., 2011; Parazzini et al., 2011), our study is, to the best of our knowledge, the first that presents a complete step-by-step approach for three-dimensional tDCS modeling, enabling a direct comparison of effect sizes. Moreover, our simulation study clearly indicated the current flow and the influence of important effects using visualized vector fields in full resolution on a glance (Fig. 4). In this way, we can formulate a guideline for efficient and yet accurate tDCS simulation: The volume conductor model needs to contain all important tissues between the electrodes and the target brain areas. Isotropic representations of the compartments skin, skull, CSF and brain gray and white matter seem to be indispensable for any tDCS simulation. The skull should be distinguished into its compacta and spongiosa compartments, if a significant volume of spongiosa is between the electrodes and the targets. White matter conductivity anisotropy modeling is important for deeper target areas, while it seems less important for

superficial targets where no significant anisotropy can be found between electrodes and targets. The latter is, however, only true under the assumption that mainly the cortical structures are sensitive to polarization, as reported by (Radman et al, 2009), who showed layer V pyramidal neuronal soma to be individually the most sensitive to polarization by optimally oriented subthreshold fields. The suprathreshold electric field action potential threshold was shown to reflect both direct cell polarization and synaptic (network) activation. In the related area of deep brain stimulation, it has recently been shown in a coupled evaluation of model and experimental data that the most realistic predictions of axonal thresholds were achieved with the most detailed model that contained diffusion-tensor based 3D tissue anisotropy and inhomogeneity and that the more simplistic models substantially overestimated the spatial extent of neural activation (Chaturvedi et al., 2010).

Further results of our study will now be discussed. We demonstrated that simulation of auditory tDCS in the most realistic head model leads to highest median current densities in brain regions close to the stimulation site; the bigger the distance towards the nearest electrode node, the smaller the median brain current density. This effect has not been reported previously. Although the pattern of peak current densities is irregular, brain regions close to the stimulation site receive highest median current densities. It thus seems that for auditory cortex stimulation, the here presented configuration is optimal and that without the availability of an individual head model, the electrodes should be placed above the auditory cortices. It should be noted that in this case both cortices are stimulated equally strong, but with reversed direction. In order to have one of the two effects (excitation or inhibition) dominate over the other, the use of different electrode sizes has been suggested. For example, in order to achieve local excitation a small anode should be placed over the target region and a large return electrode elsewhere – thus minimizing the effect of inhibition (Nitsche et al., 2007).

Our results have shown that the placement of the electrodes strongly influences the outcome of the simulation study. We have also demonstrated the importance of accurately modeling certain tissue compartments. As these structures will not be identical amongst individuals, one would ideally generate an individual head model of each patient following the guideline presented in this study. Along this line, one could adjust the electrode placement and the number of electrodes in order to optimize stimulation (Dmochowski et al., 2011). The high computational efficiency of our numerically accurate tDCS implementation using an AMG-CG solver that automatically adapts to tissue conductivity inhomogeneity and anisotropy will constitute a significant advantage for such optimization approaches.

Another obvious aspect of our simulation is that currents in lower-conducting regions tend to be oriented towards the closest higher conductive region. This effect is because of the less resistive current pathways in the higher conductive regions and has not been mentioned before.

An interesting question, raised in many tDCS experiments, is whether weak direct currents introduced to big electrodes positioned at the head surface can have therapeutic effects (Fregni and Pascual-Leone, 2007). It has been demonstrated that an electric field of about 140  $\mu\text{V}/\text{mm}$  is sufficient to enhance the firing rate of neurons (Francis et al., 2003). The strongest electric fields on the presented coronal slice in our six-compartment head models with white matter anisotropy, indeed, are about 239  $\mu\text{V}/\text{mm}$  and 167  $\mu\text{V}/\text{mm}$  for auditory and motor cortex stimulation, respectively, and therefore above this threshold. However, our study has also shown that for motor cortex stimulation the commonly used and here simulated configuration does not lead to maximal field strength in the motor cortex and suggests that achieving higher electric field strengths in the target area and bigger experimental effects of tDCS can be expected with better optimized

electrode setups (Dmochowski et al., 2011).

Not only the magnitude, but also the current density orientation is a key factor in tDCS. Nitsche and Paulus (2000) were able to demonstrate that anodal stimulation of the motor cortex enhances cortical excitability, whereas cathodal stimulation reduces it. Moreover, several tDCS experiments have shown to be significantly dependent on the polarity of the electrodes (Antal et al., 2003; Lang et al., 2004). Our results clearly showed the strong influence of especially the compartments CSF and white matter on the brain current density orientation component, underpinning the necessity of modeling these tissue compartments (at least in a homogenized isotropic way) for accurate tDCS modeling.

As described above, the quasi-static approximation to Maxwell's equations is justified for modeling in the low-frequency regime. Logothetis et al. (2007) showed with in vivo direct measurements of the cortical impedance spectrum in monkey primary visual cortex that impedance is independent of frequency, is homogeneous and tangentially isotropic within gray matter, and can theoretically be predicted assuming a pure-resistive conductor. In Bossetti et al. (2008), the authors were able to demonstrate that the quasi-static approximation is fairly good even for rapid stimulation pulses using higher frequencies (above 1 kHz). They concluded that the modeling errors were much more dependent on the conductivity than on the permittivity of the medium. Therefore, we should be able to generalize our tDCS findings to at least low-frequency (e.g., below 100 Hz) transcranial alternating current stimulation (tACS). Changing the polarity of the tDCS electrodes results in identical spatial distribution with the vector directions flipped by 180 degrees (Wagner et al., 2007). Since the problem is linear, results can be scaled to any desired input current simply by multiplying the current densities with the new current strength. Therefore, the current densities during one half cycle of tACS can be derived from tDCS by scaling and for the other half cycle by scaling and flipping the orientation by 180 degrees.

Lastly, while many other groups use commercial FEM packages, we offer with SimBio a freely available self-written code for tDCS simulation<sup>8</sup> allowing fast and accurate simulation in high-resolution inhomogeneous and anisotropic head volume conductor models.

## Outlook

This study showed that for motor cortex stimulation the standard configuration does not lead to a maximal current density at the target location. Also, both for motor and auditory cortex stimulation, the locations of the peak cortical current density in the most realistic head model used are widely distributed within the whole brain. Thus, brain regions can be unnecessarily influenced by faraway located electrodes. In future studies, we will use the fast and numerically accurate FE approach presented here to optimize the cortical current density in the target region (Rampersad et al., 2012b; Neuling et al., 2012a), while minimizing the stimulation of more remote cortical regions and ensuring safety of stimulation (Dmochowski et al., 2011). We will investigate the interplay between volume conduction and stimulation by multi-electrode schemes to predict the optimal placement, number and shape of electrodes. Using different sizes of electrodes for cathode and anode, we plan to investigate the modulation of strength of excitation and inhibition. Thereby, we want to explore the effects of anatomical pathological perturbations such as tumors, stroke or traumatic brain injury on the cortical current density distributions and thus guide clinical applications such as the treatment of

---

<sup>8</sup> SimBio tDCS code development as well as data used here will be made available after successful publication.

epilepsy, depression or stroke.

Here, we provide only the current density distribution resulting from tDCS. Although the mechanisms behind the workings of tDCS are not yet fully understood, it can be expected that functional effects are high in the areas with highest current density. In this way, current density distributions gained through volume conduction modeling can help in understanding the (lack of) effectivity of a certain stimulation set-up. This can then be used to improve the effects of stimulation by optimizing the current density distribution through adjustment of the modeling parameters. Also, the electric field distributions from modeling studies as our own are used as the input to cortical neuron (network) models that simulate the response of neurons to these fields and aim to unravel the functional mechanisms on a neuronal level (Manola et al., 2005). For both of these more practical and functional applications, the basis is a detailed volume conduction model. With this study, we have tried to provide that first step and future efforts should be made towards optimization and coupling to neuron models.

As presented in our study, details in head volume conductor modeling have a significant effect on tDCS-induced brain current density distributions. However, interindividual variability of conductivity parameters, as shown for example for the skull tissues (Akhtari et al., 2002), might cause significant modeling errors necessitating future empirical direct and indirect validation studies in animal and human subjects, respectively. Direct validation might involve combined tDCS stimulation and electric field measurements using depth electrodes in brain target areas. Such combined data might allow to directly validate simulation studies and to adjust interindividually differing tissue conductivity parameters in a way that the simulated brain current flow fits to the measured one. Similar to the recent investigations in (Neuling et al., 2012b), surface EEG can be used to indirectly validate tDCS simulations.

## Acknowledgement

This research was supported by the German Research Foundation (DFG), projects WO1425/3-1,5-1 and SFB/TRR31. The authors would like to thank Dr. H. Kugel (Department of Clinical Radiology, University of Münster, Germany) for the measurement of the MRI.

## References

- Akhtari M, Bryant HC, Mamelak AN, Flynn ER, Heller L, Shih JJ, Mandelkern M, Matlachov A, Ranken DM, Best ED, DiMauro MA, Lee RR, Sutherling WW (2002): Conductivities of three-layer live human skull. *Brain Topogr* 14:151-167.
- Antal A, Kincses TZ, Nitsche MA, Paulus W (2003): Manipulation of phosphene thresholds by transcranial direct current stimulation in man. *Exp Brain Res* 150:375-378.
- Baumann SB, Wozny DR, Kelly SK, Meno FM (1997): The electrical conductivity of human cerebrospinal fluid at body temperature. *IEEE Trans Biomed Eng* 44:220-223.
- Boggio PS, Ferrucci R, Rigonatti SP, Cobre P, Nitsche M, Pascual-Leone A, Fregni F (2006): Effects of transcranial direct current stimulation on working memory in patients with Parkinson's disease. *J Neurol Sci* 249:31-38.
- Bossetti CA, Birdno MJ, Grill WM (2008): Analysis of the quasi-static approximation for calculating potentials generated by neural stimulation. *J Neural Eng* 5:44-53.
- Camacho DL, Hopper RH, Lin GM, Myers BS (1997): An improved method for finite element mesh generation of geometrically complex structures with application to the skullbase. *J Biomech* 30:1067-1070.

Chaturvedi A, Butson CR, Lempka SF, Cooper SE, McIntyre CC (2010): Patient-specific models of deep brain stimulation: influence of field model complexity on neural activation predictions, *Brain Stim* 3:65-67.

Dannhauer M, Lanfer B, Wolters CH, Knösche T (2011): Modeling of the human skull in EEG source analysis. *Hum Brain Mapp* 32:1383-1399.

Datta A, Baker JM, Bikson M, Fridriksson J (2011): Individualized model predicts brain current flow during transcranial direct-current stimulation treatment in responsive stroke patients. *Brain Stimul* 4:169-174.

de Munck JC, Peters MJ (1993): A fast method to compute the potential in the multi-sphere model. *IEEE Trans Biomed Eng* 40(11):1166-1174.

Dmochowski JP, Datta A, Bikson M, Su Y, Parra LC (2011): Optimized multi-electrode stimulation increases focality and intensity at target. *J Neural Eng* 8:1-16.

Ferrucci R, Mameli F, Guidi I, Mrakic-Spota S, Vergari M, Marceglia S, Cogiamanian F, Barbieri S, Scarpini E, Priori A (2008): Transcranial direct current stimulation improves recognition memory in Alzheimer disease. *Neurology* 71:493-498.

Francis JT, Gluckman BJ, Schiff SJ (2003): Sensitivity of neurons to weak electric fields. *J Neurosci* 23:7255-7261.

Fregni F, Thome-Souza S, Nitsche MA, Freedman SD, Valente KD, Pascual-Leone A (2006): A controlled clinical trial of cathodal DC polarization in patients with refractory epilepsy. *Epilepsia* 47:335-342.

Fregni F, Pascual-Leone A (2007): Technology insight: noninvasive brain stimulation in neurology--perspectives on the therapeutic potential of rTMS and tDCS. *Nat Clin Pract Neurol* 3(7):383-393.

Hämäläinen M, Hari R, Ilmoniemi R, Knuutila J, Lounasmaa O (1993): Magnetoencephalography--theory, instrumentation, and applications to noninvasive studies of the working human brain. *Rev Mod Phys*, 65:1-93.

Holdefer RN, Sadleir R, Russell MJ (2006): Predicted current densities in the brain during transcranial electrical stimulation. *Clin Neurophysiol* 117:1388-1397.

Hummel F, Celnik P, Giraux P, Floel A, Wu WH, Gerloff C, Cohen LG (2005): Effects of non-invasive cortical stimulation on skilled motor function in chronic stroke. *Brain* 128:490-499.

Iyer MB, Mattu U, Grafman J, Lomarev M, Sato S, Wassermann EM (2005): Safety and cognitive effect of frontal DC brain polarization in healthy individuals. *Neurology* 64:872-875.

Jäger DET, Lutzenberger W, Birbaumer N (1987): The effects of externally applied transcephalic weak direct currents on lateralization in choice reaction tasks. *Journal of Psychophysiology* 1:127–133.

Jenkinson M, Beckmann CF, Behrens TEJ, Woolrich MW, Smith SM (2012): FSL. *NeuroImage* 62:782-790.

Jones DK (2004): The effect of gradient sampling schemes on measures derived from diffusion tensor MRI: a Monte Carlo study. *Magn Reson Med* 51:807-815.

Lang N, Nitsche MA, Paulus W, Rothwell JC, Lemon RN (2004): Effects of transcranial direct current stimulation over the human motor cortex on corticospinal and transcallosal excitability. *Exp Brain Res* 156:439-443.

Logothetis NK, Kayser C, Oeltermann A (2007): In vivo measurement of cortical impedance spectrum in monkeys: implications for signal propagation. *55(5):809-823*

Maes F, Collingnon A, Vandermeulen D, Marchal G, Suetens P (1997): Multimodality image registration by maximization of mutual information. *IEEE Trans Med Imaging* 16(2): 187-198.

Manola L, Roelofsen BH, Holsheimer J, Marani E, Geelen J (2007): Modelling motor cortex stimulation for chronic pain control: electrical potential field, activating functions and responses of simple nerve fibre



models. *Med Biol Eng Comput* 43(3):335-343.

Marshall L, Mölle M, Siebner HR, Born J (2005): Bifrontal transcranial direct current stimulation slows reaction time in a working memory task. *BMC Neurosci* 6(23): doi: 10.1186/1471-2202-6-23.

Miranda PC, Lomarev M, Hallett M (2006): Modeling the current distribution during transcranial direct current stimulation. *Clin Neurophysiol* 117:1623-1629.

Neuling T, Wagner S, Wolters CH, Zaehle T, Herrmann CS (2012a): Finite-element model predicts current density distribution for clinical applications of tDCS and tACS. *Front. Psychiatry* 3:83. doi: 10.3389/fpsy.2012.00083

Neuling T, Rach, S., Wagner S, Wolters CH, Herrmann CS (2012b): Good vibrations: Oscillatory phase shapes perception. *NeuroImage* 63:771-778.

Nitsche MA, Paulus W (2000): Excitability changes induced in the human motor cortex by weak transcranial direct current stimulation. *J Physiol* 527:633-639.

Nitsche MA, Doemkes S, Karaköse T, Antal A, Liebetanz D, Lang N, Tergau F, Paulus W (2007): Shaping the effects of transcranial direct current stimulation of the human motor cortex. *J Neurophysiol* 97:3109-3117.

Oh SH, Lee SY, Cho MH, Kim TS, Kim IH (2006): Electrical conductivity estimation from diffusion tensor and T2: a silk yarn phantom study. *Proc Intl Soc Mag Reson Med* 14:30-34.

Oostendorp TF, Hengeveld YA, Wolters CH, Stinstra J, van Elswijk G, Stegeman DF (2008): Modeling transcranial dc stimulation. *Conf Proc IEEE Eng Med Biol Soc* 2008:4226-4229.

Parazzini M, Focchi S, Rossi E, Paglialonga A, Ravazzani P (2011): Transcranial direct current stimulation: estimation of the electric field and of the current density in an anatomical human head model. *IEEE Trans Biomed Eng* 58:1773-1780.

Plonsey R, Heppner DB (1967): Considerations of quasi-stationarity in electrophysiological systems. *B Math Biophys* 29:657-664.

Radman T, Ramos RL, Brumberg JC, Bikson M (2009): Role of cortical cell type and morphology in sub-and suprathreshold uniform electric field stimulation. *Brain Stimulation* 2:215-228.

Ramon C, Schimpf P, Hauelsen J, Holmes M, Ishimaru A (2004): Role of soft bone, CSF and gray matter in EEG simulations. *Brain Topogr* 16:245-248.

Rampersad SM, Stegeman DF, Oostendorp TF (2012a): Single-layer skull approximations perform well in transcranial direct current stimulation modeling. *IEEE Trans Neural Syst Rehabil Eng*, 21(3):346-353..

Rampersad SM, Oostendorp TF, Stegeman DF (2012b): A finite element modeling approach to finding optimal stimulation configurations for tDCS. *Proceedings of the Magstim Neuroscience Conference; 2012 May 12-13; Oxford, United Kingdom.*

Rullmann M, Anwender A, Dannhauer M, Warfield SK, Duffy FH, Wolters CH (2009): EEG source analysis of epileptiform activity using a 1mm anisotropic hexahedra finite element head model. *Neuroimage* 44:399-410.

Ruthotto L, Kugel H, Olesch, J, Fischer B, Modersitzki, J, Burger, M, Wolters CH (2012): Diffeomorphic susceptibility artifact correction of diffusion-weighted magnetic resonance images. *Phys Med Biol* 57:5715-5731.

Sadleir RJ, Vannorsdall TD, Schretlen DJ, Gordon B (2010): Transcranial direct current stimulation (tDCS) in a realistic head model. *Neuroimage* 51:1310-1318.

Sadleir RJ, Vannorsdall TD, Schretlen DJ, Gordon B (2012): Target optimization in transcranial direct current stimulation. *Front Psychiatry* 3:90.

Salvador R, Mekonnen A, Ruffini G, Miranda PC (2010): Modeling the electric field induced in a high

resolution realistic head model during transcranial current stimulation. Conf Proc IEEE Eng Med Biol Soc 2010:2073-2076.

Suh HS, Kim SH, Lee WH, Kim TS (2009): Realistic simulation of transcranial direct current stimulation via 3-d high-resolution finite element analysis: effect of tissue anisotropy. Conf Proc IEEE Eng Med Biol Soc 2009:638-641.

Tuch DS, Wedeen VJ, Dale AM, George JS, Belliveau JW (2001): Conductivity tensor mapping of the human brain using diffusion tensor MRI. P Natl Acad Sci USA 98:11697-11701.

Wagner, S. (2011): An adjoint FEM approach for the EEG Forward Problem, Diploma thesis in Mathematics, Fachbereich Mathematik und Informatik, University of Münster. [http://wwwmath.uni-muenster.de/num/Arbeitsgruppen/ag\\_burger/organization/burger/pictures/DA%20Wagner.pdf](http://wwwmath.uni-muenster.de/num/Arbeitsgruppen/ag_burger/organization/burger/pictures/DA%20Wagner.pdf)

Wagner T, Fregni F, Fecteau S, Grodzinsky A, Zahn M, Pascual-Leone A (2007): Transcranial direct current stimulation: a computer-based human model study. Neuroimage 35:1113-1124.

Windhoff M, Opitz A, Thielscher A (2011): Electric field calculations in brain stimulation based on finite elements: an optimized processing pipeline for the generation and usage of accurate individual head models. Hum Brain Mapp. 34(3):923-935.

Wolters CH, Anwander A, Berti G, Hartmann U (2007): Geometry-adapted hexahedral meshes improve accuracy of finite element method based EEG source analysis. IEEE Trans Biomed Eng 54:1446-1453.

Zaehle T, Rach S, Herrmann CS (2010): Transcranial alternating current stimulation enhances individual alpha activity in human EEG. PLoS One, 5:e13766. doi:10.1371/journal.pone.0013766.

## Table and figure captions

### Table 1.

Overview of the characteristics of the five models used in our study, showing which compartments each model contains and the conductivities of each tissue type.

### Figure 1.

Current density for auditory cortex stimulation. In A2 (anode in red) and A3 (cathode in blue), the stimulating patches are shown. The left column shows current density as a vector field for the 3CI (A), 4CI (B), 5CI (C), 6CI (D) and 6CA (E) head model on a slice through the model indicated in Figures A2 and A3. The middle and right columns show the change in orientation (Ang) and magnitude (Mag) of current density that resulted from adding one feature to the model (i.e., we compare each model to the one in the row above: Figures B2/B3 show the differences between Figures A1 and B1 etc.). The color scale for the middle column indicates changes in orientation irrespective of sign. The color scale for the right column represents the factor resulting from dividing magnitudes (e.g. B1/A1), i.e., a factor of 1 (white) reflects no change. Red boxes in B1, C1, D1 and E1 indicate areas used in Fig. 4.

### Figure 2.

Current density in the brain compartments for auditory cortex stimulation. This figure is identical to Figure 1, but here the distributions are scaled to show variations in the brain. Additionally, in A2, we present a volume

rendering of the current density on the brain surface computed in the most realistic model 6CA.

### Figure 3.

Current density amplitudes in elements of the brain compartments located at a specific distance ( $\pm 2.5$  mm) to the nearest electrode are presented in a boxplot for each of the five models with auditory cortex stimulation. The black dash marks the median current density, the box comprises the upper and lower quartile and the error bars show the minimal and maximal current densities.

### Figure 4.

Selected details of the current density vector field in full resolution for auditory cortex stimulation. In Figs. 4-A,B,C and D we show magnified samples of the vector field as indicated by red boxes in Figs. 1-B1,C1,D1 and E1, respectively. Figures A show the effect of including skull spongiosa, by comparing model 3CI (A1) to model 4CI with compacta-to-spongiosa conductivity ratios of 1:3.6 (A2), 1:8.2 (A3) and 1:23 (A4). Figures B present the differences in current density distribution caused by incorporating the CSF compartment, at two locations in the 4CI (B1,B3) and 5CI (B2,B4) models. Figures C demonstrate the changes caused by including a white matter compartment, at two locations in the 5CI (C1,C3) and 6CI (C2,C4) models. Figures D present the differences that resulted from including white matter anisotropy at two locations in the 6CI (D1,D3) and 6CA (D2,D4) models. The tissue labels in each figure are adapted to the compartments contained in the presented model (for legend see Figure 1) and size-normalized cones are used to represent vector orientations and color-coding of the cones represents their amplitudes (scale identical to Fig.1).

### Figure 5.

Directional agreement (Par) between current density and the first eigenvector of the conductivity tensor in anisotropic white matter for auditory stimulation in the 6CI (A) and 6CA (B) models. Figure C shows the difference in parallelity between the two models, i.e.,  $C=B-A$ .

## Supplementary material

### Figure S1.

Current density for motor cortex stimulation. The anode (A2) was placed above the localized left primary motor cortex and the cathode (A3) above the right eyebrow. In A1, we present a volume rendering of the current density on the brain surface computed in the most realistic model 6CA. B1 shows current density as a vector field for the 6CA head model on a slice through the model indicated in Figure A2. B2 and B3 show the change in orientation (Ang) and magnitude (Mag) of current density that resulted from adding a spongiosa compartment to the low-parametric three-compartment head model.

**TABLE 1.**

Compartment	Conductivity (S/m)	3CI	4CI	5CI	6CI	6CA
Electrodes	1.4	X	X	X	X	X
Skin	0.43	X	X	X	X	X
Skull	0.01	X				
Skull compacta	0.007		X	X	X	X
Skull spongiosa	0.025		X	X	X	X
CSF	1.79			X	X	X
Brain	0.33	X	X	X		
Brain gray matter	0.33				X	X
Brain white matter	0.14				X	
Brain white matter	anisotropic					X

**Figure 1.**

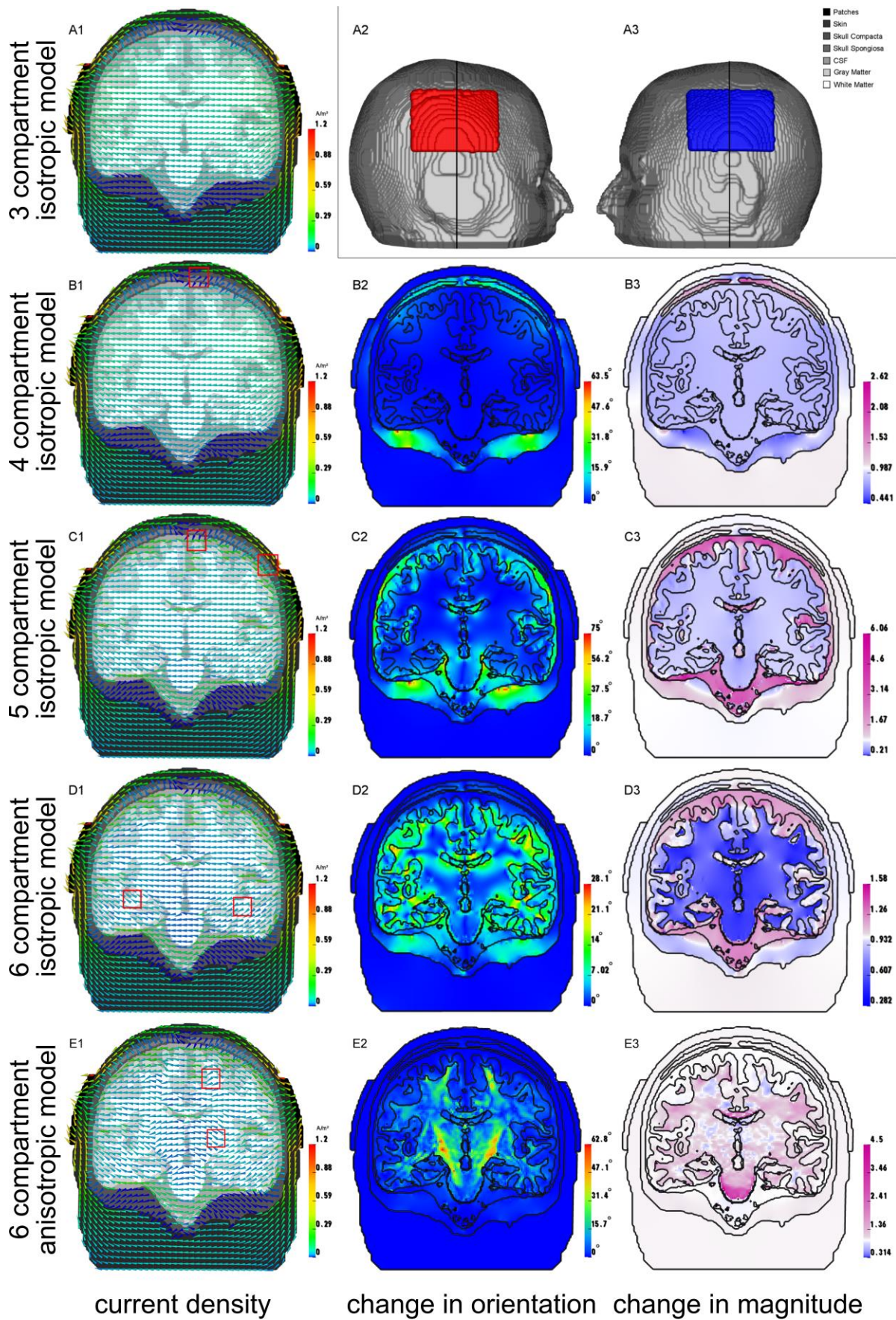




Figure 2.

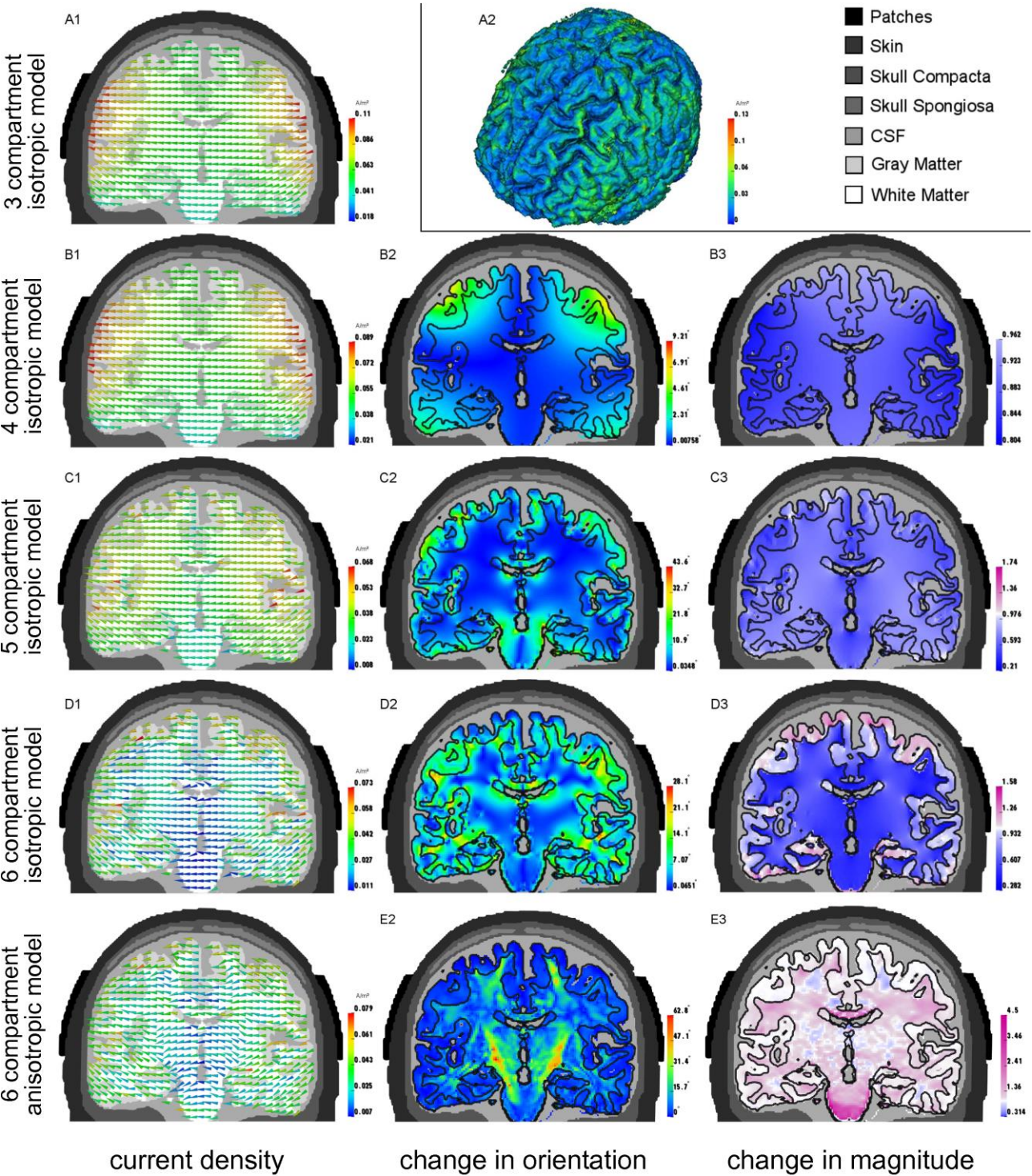


Figure 3.

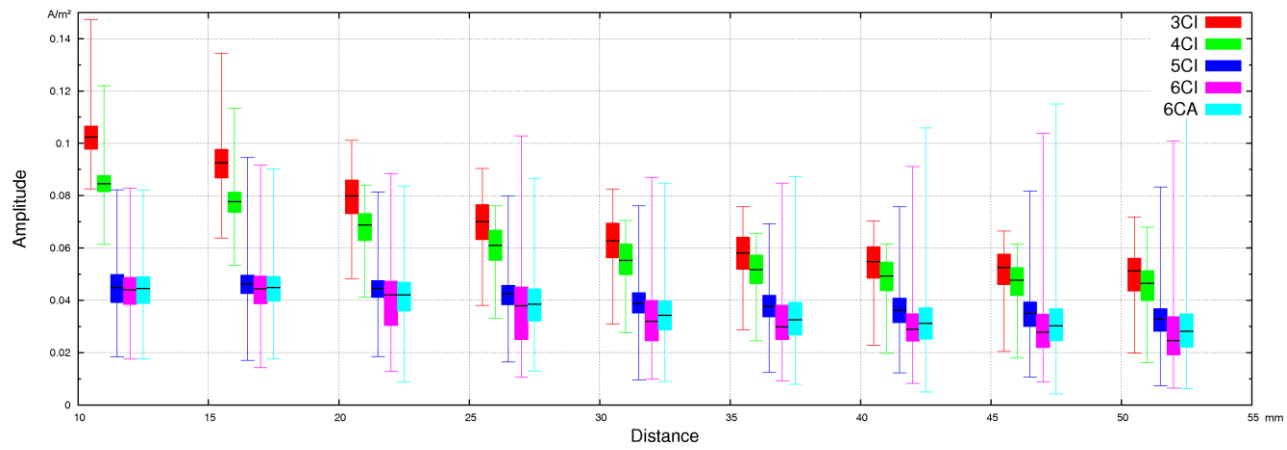


Figure 4.

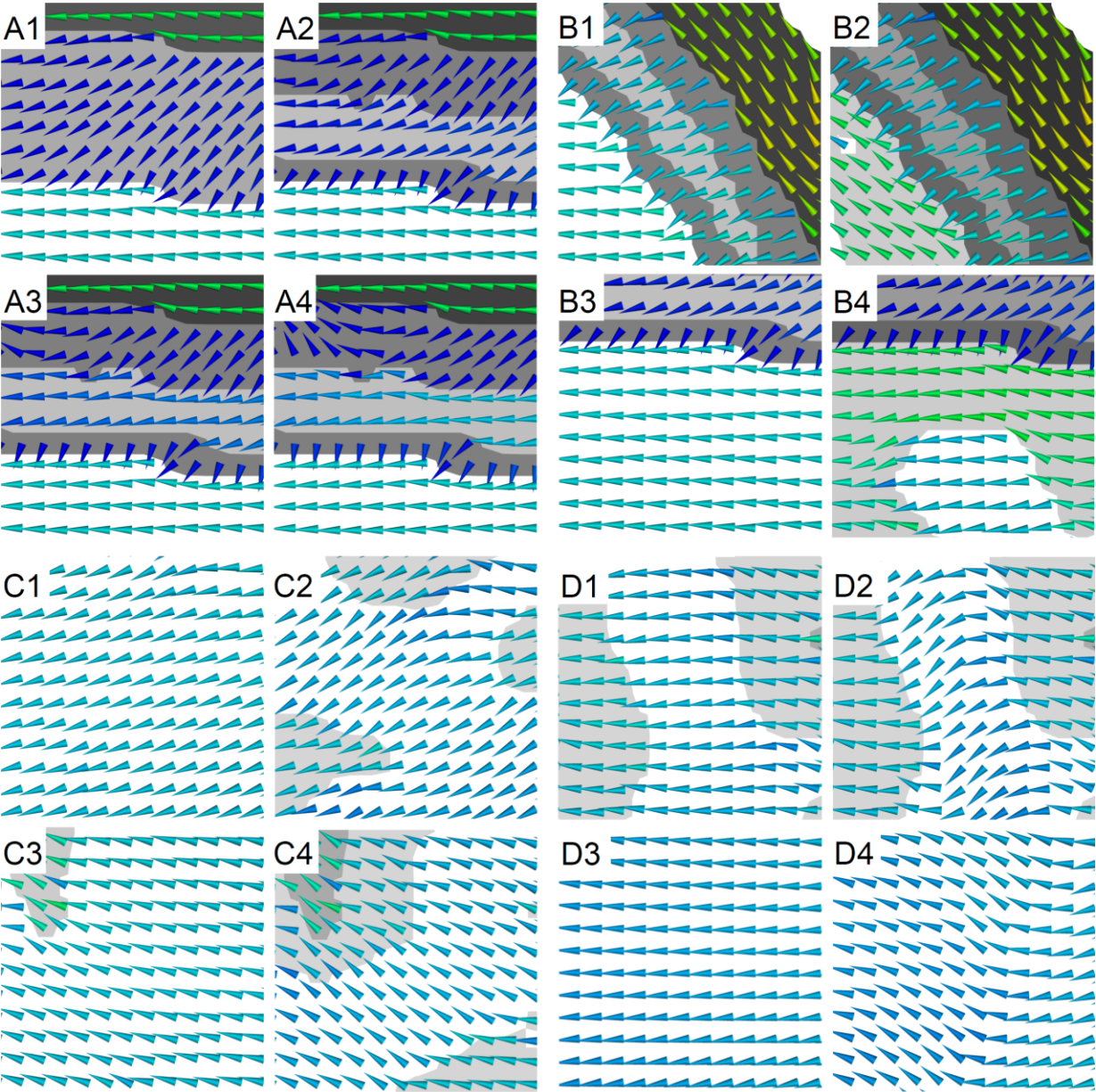




Figure 5.

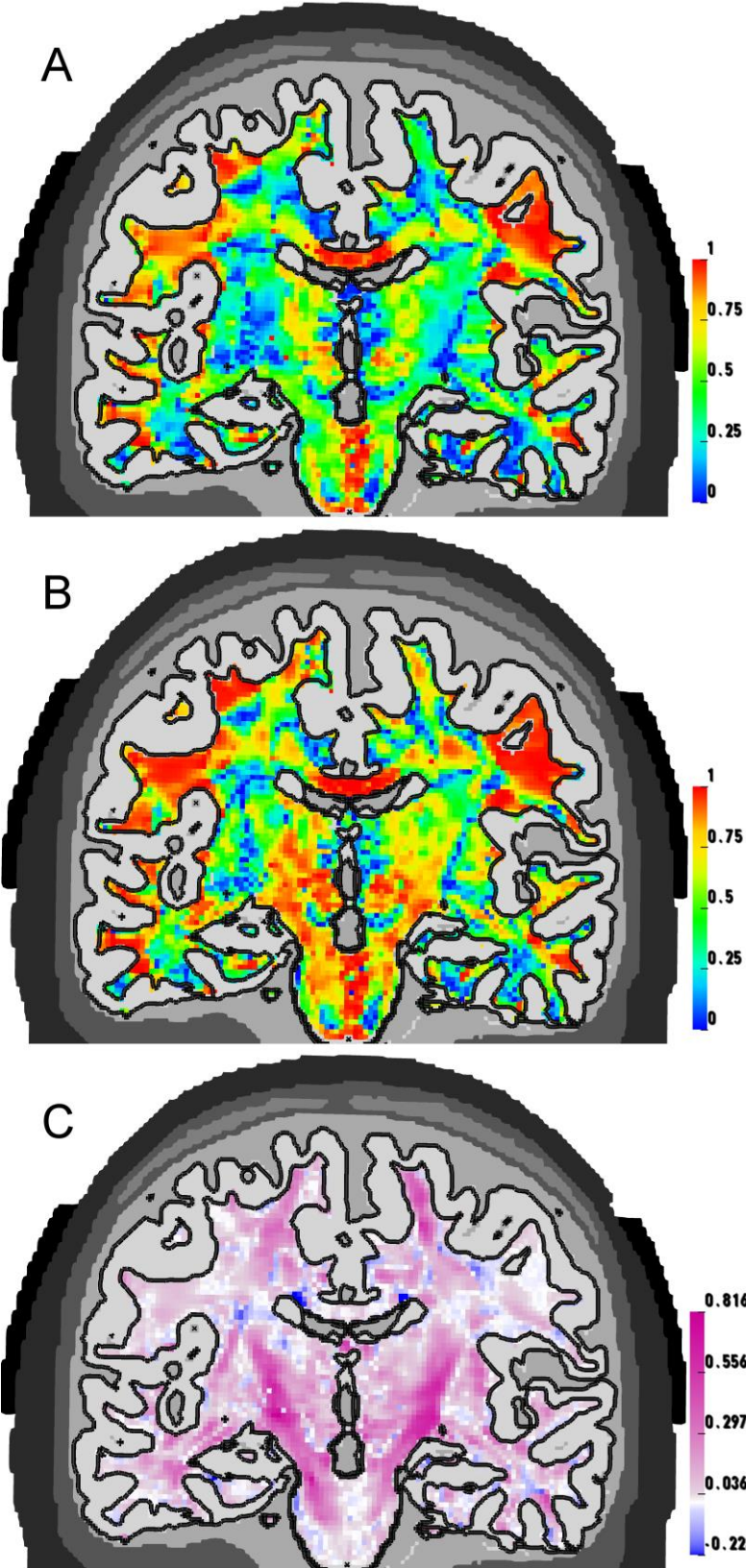


Figure S1.

